This is a research manuscript entitled “The miscibility of Calcium Silicate Perovskite and Bridgmanite: A single phase perovskite in hot, iron-rich regions” by Joshua M. R. Muir[1] (j.m.r.muir@mail.gyig.ac.cn), Andrew Thomson and Feiwu Zhang[2] (feiwuzhang@mail.gyig.ac.cn). This is a non-peer reviewed manuscript which has been submitted for publication in Earth and Planetary Science Letters. Subsequent versions of this manuscript may have slightly different content. If accepted for publication the final version will be available via the Peer-reviewed publication link.

The miscibility of calcium silicate perovskite and bridgmanite: A single perovskite solid solution in hot, iron-rich regions

Joshua M. R. Muir[1*], Andrew R. Thomson[2], Feiwu Zhang[1†]

1) Institute of Geochemistry, Chinese Academy of Sciences, 99 West Lincheng Road, Guiyang, Guizhou 50081, China

2) Department of Earth Sciences, University College London, London WC1E 6BT, UK.

[*] j.m.r.muir@mail.gyig.ac.cn

[†] zhangfeiwu@mail.gyig.ac.cn

Abstract

Calcium silicate perovskite and bridgmanite are two phases believed to coexist throughout the lower mantle, which at some temperature, at least theoretically, dissolve into each other to form a single perovskite solid solution ($Ca_xMg_{1-x}SiO_3$). This may have large seismic and geochemical implications due to the changes in density, elasticity and element partition coefficients between single and mixed phase perovskites. DFT Molecular Dynamics has been used to estimate the miscibility of bridgmanite and calcium perovskite at pressures between 25 and 125 GPa. Results at temperatures up to 2500 K indicate mixing is limited to within 4% of the pure endmembers without additional intrinsic defects present, i.e. < 4% $CaSiO_3$ is miscible in $MgSiO_3$ and vice versa. Therefore, in a simplified lower mantle chemistry extensive $MgSiO_3$-$CaSiO_3$ solid solution is not expected to occur. However, a simple model was employed to test whether the presence of other elements might influence this mutual solid solution and it was demonstrated that if sufficient concentrations (> 1 at.%) of additional elements are present then miscibility may become favourable. Of the elements likely to be present at these concentrations it appears that ferrous iron promotes, whilst aluminium inhibits, a single-phase perovskite solid solution. To a lesser extent ferric iron may both increase and decrease perovskite miscibility. Modelling for realistic mantle compositions suggests that basaltic lithologies will always retain two perovskite components, whereas a single perovskite

solid solution may be preferred in hot and/or iron-rich pyrolytic bulk compositions near the base of the lower mantle. Static calculations indicate perovskite miscibility may cause pyrolytic lithologies (with 12.5% $CaSiO_3$) to possess lower density (-0.14-0.25%), V_s (-1.5-3.5%) and V_p (-0.5-1.2%), and higher V_Φ (+0.00-0.75%) than predicted for assemblages containing two perovskites. These seismic changes, while preliminary, are similar to those observed in the LLSVPs which are also regions that are likely hotter than the surrounding mantle and thus possess conditions promoting the formation of a single perovskite phase.

1. Introduction:

At depths beyond 600-700 km perovskite (ABO_3) solutions will predominate in both ultra-mafic and mafic lithologies and control their physical attributes (Irifune and Ringwood, 1993, O' Neill and Jeanloz, 1990, Ono et al., 2004a, Hirose et al., 2017). In the lower mantle the two perovskite phases are $CaSiO_3$ (ca-pv) and $MgSiO_3$ (bdg). While work has been done to elucidate the seismic behaviour of both bdg and ca-pv (Hirose et al., 2017, Marquardt and Thomson, 2020) in order to understand their behaviour and effect on the lower mantle, these phases may not always exist as separate phases. Despite the large size difference between Mg^{2+} and Ca^{2+} cations, it is possible that complete $MgSiO_3$-$CaSiO_3$ miscibility will occur at sufficiently high temperatures, such that lower mantle assemblages only possess one perovskite phase. Previous experimental studies have reported occasional lower mantle assemblages containing only one perovskite phase (for example Creasy et al. (2020), Gu et al. (2016), and Armstrong et al., 2012), which could indicate the occurrence of miscibility at high temperature. Since an intermediate phase would likely have different seismic properties from a mechanical mixture of the endmembers it is essential to establish whether this two-phase chemical mixing is possible at lower mantle conditions.

The solubility of Ca into bdg and Mg into ca-pv has been studied experimentally, although these are limited so far to maximum temperatures of 2000 K and pressures of 100 GPa (Irifune et al., 2000, Irifune et al., 1989, Tamai and Yagi, 1989, Fujino et al., 2004, Armstrong et al., 2012). At these conditions it has generally been found that there is only a small solubility of these phases into each

60 other at lower mantle conditions (<~1.5% at 25 GPa and 2000 K rising to ~10% at 55 GPa and 2000 K).
61 Theoretically Jung and Schmidt (2011) found the solubility of Ca in bdg to be ~0.5 % at 2000 K and 25
62 GPa while Vitos et al. (2006) found this solubility to be around an order of magnitude higher. In
63 both theoretical papers solubility decreased with pressure in contrast to experimental results
64 (Armstrong et al., 2012, Fujino et al., 2004) which identified strongly increasing solubility with
65 pressure**.** In both theoretical and experimental cases solubility increases markedly with temperature.
66 From the experimental studies of Irifune et al. (2000), Fujino et al. (2004) and Armstrong et al.
67 (2012) it is clear that Ca-pv and bdg exist as separate phases in the shallow portions of the lower
68 mantle. The strong pressure dependence on mixing seen in Fujino et al. (2004) and Armstrong et al.
69 (2012) suggests that at deeper and hotter portions of the lower mantle, beyond the pressures and
70 temperatures of these experiments, a complete solid-solution may be stable. Further investigation
71 of this potential miscibility is required to both clarify the mineral structure of perovskites at deep
72 lower mantle conditions and to resolve the differing predictions of theory and experiments on the
73 pressure effect of mutual solubility.
74 Another factor which needs to be considered is the presence of contaminants (intrinsic defects)
75 and their effect on phase miscibility. Both Ti (Armstrong et al., 2012) and Fe (Fujino et al., 2004)
76 have been shown to increase the mixing of these two phases but it is unclear what elements are
77 important and how big of an effect these elements have on the overall miscibility. Additionally,
78 Creasy et al. (2020) observed a single phase perovskite with a composition containing 18 ± 2 mol%
79 $CaSiO_3$ component alongside an additional 0.59 cations of Al, Fe^{2+} and Fe^{3+} per formula unit
80 (assuming ABO_3 stoichiometry).
81 In this work we use Density Functional Theory (DFT) to probe the mutual solubility of Ca-pv and
82 bdg, with and without intrinsic defects, up to pressures and temperatures corresponding to the D''
83 region adjacent to the core-mantle boundary (125 GPa and 3000 K). We build a model of Ca-pv and
84 bdg miscibility and speculate as to whether or not this suggests a single perovskite solid solution
85 might be stable at depth within the lower mantle. Finally, we conduct static (0 K) calculations to

86 estimate the seismic signature of a single-phase perovskite relative to a mechanical mixture of Ca-Pv
87 and brg.
88
89 ## 2. Methods
90 *2.1 Mixing Thermodynamics*
91 To determine whether two phases mix we determine the thermodynamic properties of the
92 following reaction:
93 $$xCaSiO_3 + (1-x)MgSiO_3 \rightarrow Ca_xMg_{1-x}SiO_3$$ Reaction 1
94 Reaction 1 is for the pure end members. Defect elements can be introduced later by adding
95 them to both sides of the reaction.
96 The Gibbs energy of this mixing reaction is defined by:
97 $$\Delta G_{mix} = \Delta H_{mix} - T\Delta S_{mix}$$ Equation 1
98 where ΔH_{mix} is the enthalpy of mixing, T is the temperature, ΔS_{mix} is the entropy of mixing and
99 ΔG_{mix} is the free energy of mixing. Mixing will occur when ΔG_{mix} is negative. ΔS_{mix} is broken into two
100 components ($\Delta S_{mix} = \Delta S_{vib} + \Delta S_{config}$); ΔS_{vib} represents the vibrational entropy and ΔS_{config} represents
101 the configurational entropy. ΔG_{mix} will subsequently be determined in two parts. S_{vib} will be
102 determined using molecular dynamics and ΔH_{mix} and ΔS_{config} will be determined using static
103 calculations.
104 Calculations were performed across a wide range of discrete *PT* conditions and interpolated to
105 create a model covering conditions throughout the lower mantle. Molecular dynamics calculations
106 were run at 25, 75 and 125 GPa and temperatures of 1000, 2000 and 3000 K. Energies were
107 determined at Ca#=0, 25, 50 and 100 where Ca# is Ca/(Ca+Mg) in the entire system. For a 2-
108 perovskite phase assemblage Ca# defines the relative phase proportion of $CaSiO_3$ expected. Static
109 calculations (used to determine ΔH_{mix} and ΔS_{config}) were performed with Ca# of 0, 12.5, 25, 50, 75,
110 87.5 and 100 and at pressures of 25, 75 and 125 GPa (additional pressures for ΔH_{mix} are shown in

111 Table S2). All pressures are presented uncorrected, see the supplementary methods for more
112 information.

113 To calculate G_{mix} at specified *T*, *P* and *Ca#* we used the following scheme. First at each pressure
114 (25, 75 and 125 GPa), temperature (1000, 2000 and 3000 K) and Ca# (0, 25, 50 and 100) we
115 calculated *G* of the products and the reactants. Polynomials were fitted to the change in ΔG_{mix} as a
116 function of Ca# (e.g. Figure S1) followed by pressure at each temperature. Application of these
117 functions allows calculation of ΔG_{mix} at any given Ca# and pressure. Subsequently, polynomials were
118 fitted as a function of T (a sample is shown in Figure S2) to determine the ΔG_{mix} of the reaction at the
119 T of interest. The fits across P and T are relatively linear and are likely reliable at middling Ca# values
120 where there are large energy differences between the mixed and unmixed components and where
121 mixing is controlled by configurational entropy which is well constrained by the Boltzmann entropy.
122 Energy varies strongly as a function of Ca# and inaccuracies in Ca# extrapolation could lead to large
123 errors in G_{mix}. The G of the points at Ca#=25 fit near exactly to a curve of G vs Ca# plotted with
124 points at Ca#=0, 50 and 100 as shown in Figure S1 which suggests that a polynomial fit of G vs Ca# is
125 adequate. This fitting likely breaks down at extremely high and low Ca# values which is important for
126 harzburgite but as shown in Table S1 a solid solution model returns near identical answers and the
127 error in the molecular dynamics is much more important.
128
129 *2.2 Computational Details*
130 For these calculations we used the VASP code version 5.4.4 (Kresse and Furthmuller, 1996b,
131 Kresse and Furthmuller, 1996a). This is a density functional theory approach where planewave
132 pseudopotentials are used to simulate supercells which represent infinite crystals. The PBE (Perdew
133 et al., 1996) exchange correlation functional was used alongside the included VASP PAW potentials
134 (Kresse and Joubert, 1999). The valence electron shells used were Ca: 3s, 3p, 4s; Mg 3s, 3p; Si 2s, 2p;
135 O 2s, 2p. Two different sets of calculations were performed, both at static conditions and using
136 molecular dynamics. Static calculations had planewave cut-offs of 850 eV, k-point grids of 4x4x4 in a

Monkhorst Pack grid (Monkhorst and Pack, 1976). Energies were relaxed to within 10^{-5} eV and forces between atoms were relaxed to below 10^{-4} eV/Å. For molecular dynamic runs the gamma point was used with cut-offs of 600 eV and relaxed to within 10^{-4} eV**.** 80 atom unit cells were used (2x2x1) for *Pbnm* and *I*4/*mcm* structures and 40 atom unit cells (2x2x2) for $Pm\bar{3}m$ structures, except for during calculation of the configurational entropy as noted below.

Elasticity calculations, on 80 atom unit cells, at static conditions used the same cut-offs listed above. $MgSiO_3$ was supposed to assume the *Pbnm* spacegroup, $CaSiO_3$ took the *I*4/*mcm* structure and the single-phase solid solution with Ca#=6.5, 12.5, 25 and 50 was assigned the *Pbnm* spacegroup. An online script (https://github.com/andreww/elastic-constants) was employed, which calculates elasticity via the stress strain method whereby small stresses are applied in different directions to the unit cell depending upon its space group. From the resulting strain tensor the elastic constants are determined by fitting stress-strain curves and solving for $\sigma_{ij} = c_{ijkl}\varepsilon_{kl}$, where σ is stress and ε is strain. This assumes that our strain is small enough that infinitesimal strain theory applies. For orthorhombic structures 3 distortions (strains in different directions ε_{kl}) are required and 2 for tetragonal structures. For each distortion direction 4 strain points were used corresponding to ε values of 0.01, 0.02, -0.01 and -0.02.

2.3 Phases:

$MgSiO_3$ is usually in the orthorhombic *Pbnm* structure (Zhang et al., 2013). There is much debate about the crystallographic structure of $CaSiO_3$ in the lower mantle (e.g. Stixrude et al. (2007), Sun et al. (2014), Shim et al. (2002), Ono et al. (2004b), Uchida et al. (2009), Komabayashi et al. (2007) and Kurashina et al. (2004)), but following Stixrude et al. (2007) and Sun et al. (2014) we assume $CaSiO_3$ possesses either the cubic $Pm\bar{3}m$ or the tetragonal *I*4/*mcm* structures. For more discussion of $CaSiO_3$ phases see the supplementary methods. All systems (end members and mixtures) were calculated in all 3 of these symmetry groups. Interpolations across Ca# and temperature were done for all 3 symmetry groups and then at any specific composition and temperature point the lowest energy structure was chosen. For Mg end members the *Pbnm* phase dominated, whereas the

*I*4/*mcm* or $Pm\bar{3}m$ phases were dominant for Ca end members, with the $Pm\bar{3}m$ phase favoured by high temperatures. The single-phase solid solution perovskite generally adopted the *Pbnm* structure with this always being adopted when Ca#=25 or 50. This preference for a *Pbnm* structure in the mixed phase is consistent with previous experimental and theoretical observations of Armstrong et al. (2012) and Jung and Schmidt (2011) respectively**.**

To test whether post-perovskite phases were promoted by phase mixing, calculations were run on a mixed phase with a *Cmcm* structure and Ca#= 50 at 125 GPa but this post perovskite phase was found to be higher in energy than the *Pbnm* phase at all tested temperatures (1000, 2000 and 3000 K).

2.4 Molecular Dynamics:

To determine the vibrational entropy of each system a Velocity-Autocorrelation Function (VACF) method was used. More accurate methods, e.g. thermodynamic integration, are possible but because ΔG_{mix} values are fairly large in magnitude the accuracy of these methods was presumed to be unnecessary. Details of this are given in the supplementary information.

All molecular dynamics runs were performed on 80 atom (2x2x1) cells (for *Pbnm* and *I*4/*mcm*) or 40 atom (2x2x2) cells for $Pm\bar{3}m$ structures. To ensure these cell sizes were sufficient for convergence to be achieved, additional tests were also run a test on larger cells at 125 GPa and 2000 K; a 160 atom cell (2x2x2) for *Pbnm*-structured $MgSiO_3$ and $Mg_{0.5}Ca_{0.5}Si0_3$ and a 160 atom (2x2x2) cell for *I*4/*mcm*-structured $CaSiO_3$. The differences in energy between 80 atom and 160 atom unit cells were < 0.40 meV/atom for $MgSiO_3$, < 0.51 meV/atom for $Mg_{0.5}Ca_{0.5}Si0_3$ and < 0.58 meV/atom for $CaSiO_3$. Overall, this corresponds to a change of less than 0.51 meV/atom in ΔG_{mix} for reaction 1, implying that good convergence is achieved using 80 atom unit cells.

The error in the energies obtained using molecular dynamics were calculated for each individual run using the method of Flyvbjerg and Petersen (Flyvbjerg and Petersen, 1989), and were less than 1.5 meV/atom in all cases. The effect of propagating these errors is explored in Table S1 but we find that within 2σ Tmix does not vary by more than 50 K for any Ca#.

2.5 Configurational Entropy:

To determine the configurational entropy of perovskite solid solutions we calculated the energy of different configurations of Mg and Ca in the unit cell. As the number of possible configurations are proportional to N factorial, 80-atom cells are too large to test all possible configurations. However, the energy difference of each configuration is independent of the simulation cell size, such that the only disadvantage of using a smaller simulation cell when determining configurational entropy is that some configurations may be somewhat under- or over-sampled. A smaller simulation cell consisting of 40 atoms (2x2x1 unit cells) for compositions with x=0.25, 0.5 and 0.75 (for $Ca_xMg_{1-x}SiO_3$) will not contain every configuration that would be assessed using 80 atoms, however, it does contain a sufficiently large number of configurations such that the configurational entropy in an infinite crystal is adequately approximated. For solid solutions with x=0.125 or 0.875 use of an 80 atom simulation cell was required to ensure sufficient unique configurations were probed. Thus we used a 40 atom cell for x=0.25, 0.5 and 0.75 and an 80 atom cell for x=0.125 and 0.875. For each of these configurations we calculated the enthalpy for every possible configuration of Ca and Mg in the cell and calculated the configurational entropy using the Gibb's entropy function with details given in the supplementary methods. Our method likely underestimates the configurational entropy but as explained in the text using the maximum possible configurational entropy (the Boltzmann entropy) makes little difference to our results. This means that the deviation of our entropy from the perfect Boltzmann entropy value is not a significant control on the miscibility and any underestimation is not a significant control on our results.

3. Results:

3.1 Enthalpy and Entropy of Mixing

The miscibility of any two endmembers can be assessed using Equation 1, which evaluates the change in Gibbs energy (ΔG_{mix}) were full miscibility to occur. For any two substances ΔS_{mix} will be

positive, since a single miscible solid-solution will always have more available atomic arrangements than two coexisting endmembers. Assuming that the two endmembers are naturally immiscible at low temperature, ΔH_{mix} is also positive because energy is required to overcome their natural aversion to mixing. As the reaction occurs when ΔG_{mix} is negative, miscibility can be achieved with increasing temperature as $-T\Delta S_{mix}$ overcomes the positive ΔH_{mix}, providing this occurs prior to melting or dissociation of the original endmember phases. Mutual solubility of the two endmembers occurs at thermodynamic equilibrium, when $\Delta G_{mix} = 0$, at a temperature subsequently denoted T_{mix}. The temperature T_{mix} defines the maximum extent of the two-phase solvus.

The values of ΔH_{mix}, ΔS_{config} and ΔS_{vib} calculated as described above as a function of pressure are reported in Tables S2, S3 and S4 respectively. Inspection of these parameters reveals that ΔH_{mix} increases with pressure, ΔS_{config} only slightly increases and is almost insensitive to pressure increases and ΔS_{vib} has a complex relationship but generally increases with pressure. The increase in ΔH_{mix} with pressure occurs despite the single perovskite solid solution being less dense than a mechanical mixture of two phases (Table 1). This is likely due to the energy required to replace Mg^{2+} with larger Ca^{2+} cations, which increases with pressure as the perovskite A-site is compressed.

Combining the pressure systematics of ΔH_{mix}, ΔS_{config} and ΔS_{vib} demonstates that increases in ΔH_{mix} are overcome by the growth in entropy terms at high pressure, such that T_{mix} is observed to fall as pressure increases (Figure 1). This observation is consistent with the results of Fujino et al. (2004) and Armstrong et al. (2012). Inspection suggests it is the increasing magnitude of ΔS_{vib} that is responsible for Equation 1 becoming negative and promoting a single perovskite solid solution with pressure. This is in contrast with two previous theoretical studies, which both concluded that T_{mix} should increase with pressure (Jung and Schmidt, 2011, Vitos et al., 2006). However, as both these studies only estimated ΔS_{vib} without calculating it, the increase in T_{mix} with pressure and the high values for T_{mix} (> 4000 K) obtained within these studies appear to have been caused by poor constraint on value and the changes in ΔS_{vib} with pressure.

240 Calculated values for ΔS_{config} vary slightly from ideal Boltzmann entropy values, but this effect is
241 small. If we were to replace all ΔS_{config} values with those of an ideal Boltzmann mixture, T_{mix} would
242 vary by less than 75 K in all cases (less than 10 K in most occurrences). Thus, it is concluded that Ca
243 and Mg are largely interchangeable between various different sites such that ideal mixing, as far as
244 configurational entropy is concerned, occurs.

245 *3.2 Mixing in the $CaSiO_3$-$MgSiO_3$ system:*

246 Figure 1 plots the calculated $MgSiO_3$-$CaSiO_3$ phase diagram as a function of temperature at
247 pressures of 25, 75 and 125 GPa (an alternative rendering as a phase diagram is shown in Figure S3).
248 At each pressure we identify two regions in the miscibility loop structure. At low, or high, Ca#
249 (where Ca# is Ca/(Ca+Mg)) the miscibility boundary changes rapidly with the temperature in
250 response to the control of ΔH_{mix} and ΔS_{vib}. At intermediate Ca# values, the miscibility curve plateaus,
251 and there is little continuing change with temperature as this region is controlled by ΔS_{config}.

252 In the $CaSiO_3$-$MgSiO_3$ system the calculated solubility of Ca in bdg and Mg in ca-pv at 25 GPa and
253 2000 K are ~ 0.41% and ~ 0.18% respectively, while T_{mix} (the temperature required for complete solid
254 solution) is ~ 3170 K. At 75 GPa the calculated solubilities at 2000 K increase to ~ 0.52 and ~ 0.13%
255 respectively, with T_{mix} falling to ~ 3050 K. At 125 GPa the calculated solubilities at 2000 K are ~ 1.12
256 and ~ 0.07% respectively, with T_{mix} ~ 2740 K. At 2000 K increasing the temperature has little effect
257 on solubility. At higher temperatures increasing the pressure causes a large increase in solubility.
258 This high temperature effect is due to the different plateau temperatures seen in Figure 1. In the
259 theoretical study of Jung and Schmidt (2011) the solubility of Ca in bdg was found to be 0.5% and
260 the solubility of Mg in Ca-pv to be much lower at 25 GPa and 2000 K which is similar to our work.
261 Experimentally Fujino et al. (2004) found solubilities of ~ 1% Ca in bdg and 4% Mg in ca-pv at 2273 K
262 and 30 GPa, Irifune et al. (2000) found 1.1-1.5% solubility of Ca in bdg and 2.1-3.2% of Mg in Ca-pv at
263 25 GPa and 1973 K and Armstrong et al. (2012) found 4.7% solubility of Mg in Ca-pv at 53 GPa and
264 2000 K. These experimental results all show higher solubility than we predict here. Small solubilities
265 are the hardest to constrain as they occupy the steepest part of Figure 1. This could come either

through problems with our fitting model which extrapolates down to low Ca# numbers or through inaccuracies in our calculations. As shown in Table S1 a Margules fitting model provides the same result as our polynomial fit but more fitting parameters at lower Ca# could possibly change this outcome. At these low solubilities the main constraint is not fitting but the small energies involved. The difference between a solubility of 0.41% (predicted by us) and 1.25% at 2000 K and 25 GPa (measured by Irifune *et al.* 2000) is a shift in energy of R1 of less than 1 meV/atom. This is beginning to approach the limits of MD accuracy particularly without very long and costly calculations. The difference in solubility between experiment and our calculations are likely to be much larger at small solubilities where the mixing curve is steep (Figure 1) than at large solubilities on the order of mantle phase compositions where the mixing curve flattens out and small energy differences in mixing are unimportant. Thus at lower mantle conditions our solubilities should be better constrained. The small energy differences between different solubilities at very low or very Ca# means that these solubilities are also hard to constrain in experiment as small temperature or pressure differences should have large effects on the solubility. Experimentally there could be thermal lags across the system, particularly at interfaces of mixing where heat may not transfer well. If experimental temperatures at the mixing interface are higher than recorded in the sample that could explain these differences in solubility. Different experiments use different pressure scales (Armstrong *et al.* (2012) and Fujino *et al.*(2004) use ruby fluorescence, Irifune *et al.* (2000) Au) and the calibration of these can sometimes lead to significant differences (see for example Ye et al. (2018)) which may cause additional differences. Our pressures in this study are uncorrected for the systematic pressure errors in DFT which could lead to a shift of over -5 GPa. Compositional differences between experimental samples could also lead to solubility differences which shall be explored in the next section. Finally, another possible source of difference comes from the definition of solubility. Our study defines solubility by its thermodynamic equilibrium with no consideration of kinetics whereas the experimental studies define solubility by the disappearance of XRD or ATEM patterns. This experimental definition allows for the presence of metastable

dissolutions and problems with detection limits, both of which should increase measured solubility in the experimental case.

3.3 The Effect of Other Elements

The chemical complexity of the natural mantle means that Ca-pv and bdg are likely to contain many intrinsic defect elements when stable at lower mantle conditions. Bridgmanite crystals have been shown to be capable of hosting large (1-10 at. %) amounts of Fe and Al (Kaminski, 2017) alongside smaller quantities of several additional elements. Any additional elements, even those present in extremely small amounts, can have a large effect on ΔS_{config}, whereas only elements present in large amounts will have significant effects on ΔH_{mix} and ΔS_{vib}. As there was no conceptual model for which elements will most significantly affect the thermodynamic parameters for perovskite solubility we have employed a simple defect model allowing the effect of incorporating a large number of elements (Table 2) to be examined at 25 and 125 GPa in a bulk composition of Ca#10% Ca (a roughly pyrolytic assemblage). The simple model employed relies on the following assumptions:

1) ΔS_{vib} is unaffected by the addition of defects. Since ΔS_{vib} is most strongly dependent on long-range phonons it is unlikely to be affected by low concentration defects. Defects present in large (>5%, e.g. Al or Fe) quantities are more likely to cause a significant effect. Such effects are only evaluated through changes to ΔH_{mix} (through static calculations) and ΔS_{config}.

2) Defects follow ideal mixing, such that their effect on ΔS_{config} is ideal. Variations to ΔS_{config} are therefore only dependent upon the available number of lattice sites.

3) The effect of defects on ΔH_{mix} is linear; adding 2 iron atoms requires twice the energy of adding 1 iron atom.

4) Only one substitution mechanism is active for each defect species; defects either substitute for Mg on the A-site, Si on the B-site, undergo a coupled substitution for both Mg and Si, or exist in their most stable interstitial location (Table 2).

5) Prior to solid solution formation, it is assumed that each defect element partitions solely into either bdg or ca-pv (depending upon energy).

Using these assumptions, the effect of any defect element can be calculated by assessing the enthalpy and entropy change of all three phases (ca-pv, bdg and the perovskite solid solution). The enthalpy change associated with the incorporation of 1 defect atom per 80 atom simulation cell was calculated, which is an effective defect concentration of 6.25 atomic %. These changes in H were linearly propagated with composition, and combined with the changes in S_{config}, calculated using the Boltzmann entropy formula, to allow estimation of ΔT_{mix}.

While all five of these assumptions will break down, particularly at large concentrations of defects, this method captures two of the most significant energy changes introduced by defect elements (those on ΔS_{config} and ΔH_{mix}), and therefore permitting identification of which defect elements may significant affect ca-pv and bdg miscibility. The first assumption, that the vibrational entropy is unaffected by the presence of defects, could be erroneous especially in the presence of large amounts of defects. To test this assumption we explicitly calculated this term for a perovskite system containing an additional Fe(II) defects . The results of this calculation are given in Table 3, and demonstrate this term is small enough (<1 meV/atom at high pressure) that it can be ignored at least for ferrous iron. To test how appropriate the remaining assumptions are additional explicit calculations were also performed for the incorporation of Ti as a defect element. We calculated ΔS_{config} and ΔS_{vib} using the methods described for this study but over a range of Ti# (Ti/(Ti+Si)) values (0, 0.25, 0.5 and 1). A comparison between these full, and explicit, calculations and results of the simple model presented here are given in Table S5. Although there are differences between both predictions, our simple model used here identified the same magnitude of effect for Ti defect incorporation and should therefore allow qualitative prediction of which elements can alter perovskite miscibility and permit estimations of what concentrations of these elements may become significant.

342 Table 2 demonstrates there is no clear pattern, with charge or ionic size, for which defect
343 elements are most likely to alter T_{mix} such that individual electronic effects must be dominating
344 estimated results. Therefore, it is difficult to predict off-hand which elements will affect T_{mix}
345 significantly and in which sense. Whilst many elements increase T_{mix} others reduce ΔH_{mix} and thus
346 also T_{mix}. The most important of those which reduce T_{mix} are the noble gases (which can cause very
347 large reductions of H_{mix} due to their position as an interstitial defect). Na(I), K(I), many of the
348 transition metals in particular Co(II), Ni(II) Sc(II) and Fe(II), and 4+ cations that replace Si such as S, Ti
349 and C also reduce the temperature of miscibility. Some elements that strongly increase H_{mix} and thus
350 T_{mix} are the larger alkaline earth metals (Sr, Ba) and B. Increasing the pressure has varied effects on
351 these trends, increasing H_{mix} for some elements and decreasing it for others, but defect induced Δ
352 T_{mix} values are similar at 25 and 125 GPa. This is because the largest effect of defect elements on T_{mix}
353 is through modifying S_{config} which in this model is pressure independent. Even though defect changes
354 to H_{mix} (ΔH_{mix}) are very significant, pressure induced changes to ΔH_{mix} are largely insignificant
355 compared to changes to S_{config}. We note that whilst we have estimated the effect of many elements
356 on perovskite miscibility we have not explicitly calculated the solubility of each of these defects in
357 the solid solution at mantle conditions, the predicted effects are meant to serve as illustrative.
358 The most notable observation from this modelling is that large amounts of defects are required
359 to induce significant changes in T_{mix}. With Ca#=10, all defect atoms require a concentration greater
360 than 0.3 atomic% for T_{mix} to change by 100 K, with the required concentrations in excess of 1
361 atomic % for most elements. This is significant because most defects atoms which can be
362 incorporated in bridgmanite and Ca-pv are likely to be well below this level, allowing restriction of
363 the elements under consideration to those that are significantly abundant in the bulk mantle
364 composition or those thought to be concentrated in certain regions. Throughout the remainder of
365 this study we assume that the only elements likely to be significantly abundant to alter perovskite
366 miscibility substantially are Fe and Al. High spin ferrous Fe was estimated to decrease T_{mix} by up to
367 1000 K (Fe%=10, Ca#=10) in a pyrolytic mixture which is consistent with the observation of Fujino et

al. (2004) suggesting that additional iron increased the total solubility at a fixed temperature. In contrast Al appears to increase T_{mix} by up to 230 K (Al%=5, Ca#=10) and so somewhat counteracts the effects of ferrous iron. The presence of Al can also promote the oxidation of iron, by forming Fe-Al pairs where the iron exists as high spin on (primarily) the A site (Shim et al., 2017, Catalli et al., 2011, Kupenko et al., 2014). With the introduction of Fe-Al pairs T_{mix} is largely unaffected with T_{mix} slightly reducing by 38 K with Fe-Al%=5 and Ca#=10. Pure ferric iron (as a coupled substitution of two iron atoms replacing Mg-Si) only slightly decreases T_{mix} at low pressure and slightly increases it at high pressure.

The effect of these elements on some non-pyrolytic mixtures (i.e. varying Ca#) are shown in Table S6 and S7. At Ca# of 50 the effects of defect elements are typically reduced, such that Ca# the change in T_{mix} (ΔT_{mix}) is roughly half of what it would be in an equivalent pyrolytic system. The effect of defect elements in bulk compositions with high Ca# is similar to those with Ca#=10 (i.e. pyrolite), although the magnitude of defect element effects are slightly larger.

4. Discussion:

4.1 Single phase regions of the lower mantle

The composition of the lower mantle remains uncertain, and possible variations of Ca# are significant. Pyrolytic compositions are generally taken to possess a Ca# of 0.07-0.12 (Kesson et al., 1998, Irifune and Tsuchida, 2007, Mattern et al., 2005, Ringwood, 1991), whereas delpeted harzburgitic rocks have far lower Ca# 0.01-0.03 (Ringwood, 1991, Michael and Bonatti, 1985). Mafic lithologies, such as subducted mid-ocean range basalt (MORB), is the most Ca-enriched of the commonly considered mantle lithologies, possessing Ca# of between 0.3-0.6 (Hirose et al., 2005, Hirose and Fei, 2002, Irifune and Tsuchida, 2007, Ricolleau et al., 2010). These variations in bulk composition control the degree of miscibility required for a single-phase perovskite solid solution to form at lower mantle conditions. The required values of T_{mix} applicable to the compositional ranges

of pyrolitic, harzburgitic and MORB bulk compositions are plotted in comparison with a mantle geotherm (Ono, 2008) in Figure 2. In defect-free pyrolytic or MORB compositions, the small variations in the possible Ca# values do not substantially alter T_{mix}. T_{mix} for the most Ca-enriched and Ca-depleted pyrolytic compositions only vary by a maximum of 30 K, whereas T_{mix} for MORB compositions varies by < 5 K across the Ca# range. Due to the lower Ca-content of depleted harzburgitic mantle lithologies, small changes in the exact Ca content of the bulk composition cause significant changes in the predicted miscibility temperature according to the model employed here; e.g. T_{mix} values for Ca#=1 and Ca#=3 differ by 320 K at 25 GPa. These large differences arise because Ca# values for harzburgite occur in the region of the phase diagram where steep changes in solubility are observed, whereas those for pyrolite and MORB occur closer to the plateau regions (Figure 1). We caution that the miscibility boundary is poorly constrained at extreme values of Ca#, such that the apparent values of T_{mix} for harzburgitic compositions may be subject to significant uncertainty.

4.2 Pyrolitic Compositions

As shown in Figure 2 for a pure pyrolytic composition with no additional elements we see that it remains above the lower mantle geotherm up until the D'' at 125 GPa. Thus, pure $CaSiO_3$ and $MgSiO_3$ are not expected to form a single perovskite solid-solution at conditions of the "normal" mantle geotherm.

Figure 3 shows the predicted effect on T_{mix} of the presence of Fe and Al compositional defects by plotting the depth in the mantle that a single perovskite solid solution is predicted to become favourable along a mantle geotherm (an alternative rendering of this graph showing T_{mix} at different pressures is provided in Figure S4 and compositional variation is shown in Figure S5 and S6). Increasing the amount of Ferrous iron increases perovskite miscibility and promotes a single-phase perovskite solid solution to become stable at shallower conditions. However, the contrasting effect of Al decreasing perovskite miscibility means that for most reasonable pyrolytic compositions T_{mix} will not be strongly affected. These predictions have assumed that the formation of Fe-Al pairs is

420 favoured over ferrous iron and Al-Al pairs (Mohn and Tronnes (2016)). Alternatively, if ferrous iron
421 and Al-Al pairs dominate then the predictions are somewhat different, with miscibility expected at
422 slightly shallower conditions (Figure S5).

423 While perovskite miscibility is predicted to be unfavourable in the "normal" pyrolytic mantle, hot
424 regions such as within mantle plumes or LLSVPs, may promote formation of a single miscible
425 perovskite solid solution. Figure 4 plots the predicted perovskite miscibility depth along a
426 temperature profile that is 500 K above the regular mantle geotherm, which may represent
427 conditions occurring in LLSVPS or plumes (McNamara, 2019). At these excess temperatures,
428 miscibility of the endmember perovskite phases is more extensive and is predicted to be favourable
429 at pressure beyond ~ 80 GPa. Therefore, it is suggested that anomalously hot peridotitic regions of
430 the mantle may possess a phase assemblage consisting of only one-perovskite and ferropericlase.

431 Model predictions therefore suggest that perovskite miscibility is promoted by excess heat and
432 high iron contents. In the natural mantle the formation of such iron-rich perovskite compositions
433 may be limited by preferential partitioning of iron into coexisting ferropericlase. Predictions plotted
434 in Figures 3-4 (and all similar graphs) refer exclusively to the concentration of defect elements in the
435 perovskite phases (bdg, Ca-pv and mixed phase) which are not equivalent to the bulk composition as
436 we have not accounted for the influence of periclase. Under normal conditions iron preferentially
437 partitions into periclase relative to bridgmanite (Muir and Brodholt, 2016, Xu et al., 2017), with value
438 of $K_D^{pv\text{-}fper} < 0.5$ in the deepest portions of the mantle ($K_D^{pv\text{-}fper} = [Fe_{pv}/Mg_{pv}]/[Fe_{fp}/Mg_{fp}]$. With
439 increasing pressure iron increasing favours ferropericlase such that beyond ~80 GPa iron is likely
440 constrained << 5 % Fe whereas Al should remain relatively constant >~5 %. Thus in the normal deep
441 lower mantle iron concentration should be very limited in contrast to Al and T_{mix} values should
442 remain near their defect-free values or somewhat increased. The mixed perovskite phase also
443 favours Fe, however, and thus may compete with ferropericlase for iron which would raise the
444 effective iron concentration in bridgmanite for considering miscibility. More data is needed to
445 examine this point fully but in general Fe concentration in bridgmanite in the lower mantle is very

446 low even in iron-rich regions and thus only hot lower mantle should be a source of mixed perovskite
447 phases.
448
449 One area of the mantle that potentially is compositionally heterogeneous are the LLSVPS
450 (McNamara, 2019). While it is unclear what the compositional difference of these regions are, as
451 shown in Table 2 only differences that exceed ~1 atomic% are important to mixing of the perovskites,
452 and it remains likely that LLSVPs do not contain any defect elements at such elevated concentrations
453 other than Fe or Al. Thus when considering LLSVPs, miscibility of the two perovskite phases should
454 primarily be constrained by their elevated temperature, with a secondary effect for potential
455 changes in Fe and Al content. Any exotic compositional differences that may exist are unlikely to be
456 important for phase mixing of the perovskite. As LLSVPs are believed to be considerably hotter than
457 the rest of the mantle they are more likely to possess a miscible perovskite solid solution.
458
459 Another area where this mixing behaviour is potentially important is in the formation of a post-
460 perovskite (ppv) phase in bdg and hence on the D''. As the pressure increases beyond 125 GPa the
461 free energy of the single chemically mixed phase (Ca-pv+bdg) becomes lower than the free energy of
462 the mechanically mixed ca-pv+bdg phases and this is particularly the case with additional iron. This
463 is important because it means that the addition of Ca-pv at D'' conditions stabilises the bdg
464 perovskite structure against the ppv structure unless Ca can similarly dissolve into a ppv phase.
465 $CaSiO_3$ adopting or dissolving into a ppv structure has been suggested to be unlikely in the literature
466 (Fujino et al., 2009). As discussed in the methods we find that the mixed phase prefers a pv
467 structure to a ppv structure which is additional evidence that Ca containing crystals do not like to
468 form ppv structures. Thus at high pressures bdg in the presence of Ca-pv has two competing
469 stabilisation reactions- one to form ppv without Ca-pv and one to form the mixed pv phase with Ca-
470 pv. We shall attempt to consider how these stabilisation reactions compare.

To examine whether this is an important effect we compared our calculated energies of G_{mix} vs literature energies for the pv to ppv transition of bdg. To obtain energies for this latter transition we took the Clapyeron slope (9.56 MPa/K) and volume difference (1.78 Å) of the pv to ppv transition in bdg from Oganov and Ono (2004) and converted these to an energy difference of ~0.27 meV/Kf.u assuming an identical increase in enthalpy and volume with pressure for both phases. At 125 GPa and 2700 K (a rough value for the point where pv converts into ppv in pure bdg) G_{mix} is -13.7 meV/f.u. for a pure mixture with Ca#=10 and -6.97 meV/fu for a mixture with Ca#=10 and 8% ferrous iron and 2% Fe-Al. These values correspond to a stabilisation of the bridgmanite phase relative to the post-perovskite phase of ~2.74 and 1.40 GPa respectively. These values are approximate and a full energy minimisation needs to be performed but Ca# is unlikely to be a major control on this system. Experimental determinations of the pv to ppv phase transition in bridgmanite have shown that the transition occurs at shallower depths in MORB mantle compositions compared to pyrolytic compositions (Ohta et al., 2008, Tateno et al., 2009, Grocholski et al., 2012) despite MORB compositions having more Ca than pyrolytic compositions. If Ca had a major effect on this transition then MORB compositions would see the pv to ppv transition occurring at deeper depths as Ca stabilises the pv structure relative to the ppv structure. An explanation for this anomalous behaviour is that other elements have a larger effective on the pv to ppv transition. The most likely element is Al which has high concentration in MORB mantle and thus stabilises the ppv phase despite the effect of Ca (Grocholski et al., 2012).

4.3 Harzburgitic Compositions

As shown in Figure 2 harzburgitic compositions behave largely like pyrolytic compositions but they have smaller values of T_{mix}, and should therefore become miscible at shallower depths. Varying the Ca# ratio has a very large effect on T_{mix} in harzburgite because the possible Ca# values exist in an even steeper range of the solubility curve and thus the amount of Ca that is present is extremely

important. The effect of other elements on harzburgite mixing is shown in Figure S7 and S8 but are similar to pyrolite in that ferrous Fe increases mixing sharply.

4.4 Basaltic Compositions

A final case to consider is a descending slab or unmixed mantle with a more MORB-like composition. As is shown in Figure 2 this has quite different behaviour to the pyrolytic case. T_{mix} is considerably higher in the MORB case and is considerably above the temperature of descending slabs (the coldest slab adiabiat is shown in Figure 2). Varying the Ca# ratio has little effect on mixing in basaltic compositions as they exist in the plateau region of Figure 2 and thus all basaltic compositions should behave largely similarly. The effect of defect elements is shown in Figure S9-S10. Even with extremely enriched amounts of ferrous d iron (20%) T_{Mix} remains nearly 600 K above the temperature of the coldest adiabiat at 125 GPa and thus phase mixing does not occur in descending slabs even in cases of extreme iron enrichment. MORB that exists at geotherm temperatures (for example from unmixed pyrolite) will also not mix except in the presence of large amounts of ferrous iron (>5%) with little Al which is unlikely as basalts are generally high in Al.

While we predict no mixing in the lower mantle for MORB our predicted mixing temperatures for MORB contradict an experimental study where MORB was heated until it melts at varying pressures up to CMB pressures and no sign of phase mixing was observed in the XRD spectra (Pradhan et al., 2015)**.** While this sample contains large amounts of Al which will increase T_{mix} our predicted T_{mix} is still well below the melting temperature at high pressure. In this study samples were heated for 30 minutes which is similar to the heating times for experiments where mixing has been observed (Armstrong et al., 2012, Fujino et al., 2004, Irifune et al., 2000). This suggests generally that mixing had enough time to occur in these melting experiments and the lack of any mixed phase formation was not a kinetic effect. One possible solution to this is that these melting experiments had large amounts of Fe and Al when compared to the other studies and these elements would need to diffuse before and during mixing which could delay the formation of a single phase as this diffusion is slow. Alternatively our simple model may underestimate the effect

522 of some elements, most likely Al, in raising T_{mix} and the full effect of these elements needs to be
523 modelled with MD or experimentally.

524 *4.5 Seismic Effects*

525 The calculations presented above suggest that bdg and ca-pv may become miscible in hot and/or
526 chemically anomalous regions of the deep lower mantle. If such miscibility occurs the seismological
527 properties of the single-phase perovskite solid solution may be significantly different to that of a
528 two-perovskite phase assemblage, such that is instructive to consider whether miscibility will alter
529 the geophysical signature of these mantle portions.

530 The density of a single-phase perovskite solid solution of pyrolytic composition is compared with
531 that of a mechanical mixture of bdg and ca-pv in Table 1. A single perovskite solid solution is less
532 dense than an equivalent mechanical mixture, but this density difference is small (<0.26%) and
533 therefore unlikely to have large effects without associated changes in the bulk and/or shear moduli.
534 In Figure 5 we consider the elasticity of these structures.

535 These considerations are not completely straightforward as, firstly, throughout several studies
536 published across the literature the elasticity of the Ca-pv phase has proven to be difficult to
537 determine, using both theoretical and experimental techniques (Thomson et al., 2019, Kawai and
538 Tsuchiya, 2015). Secondly, all considerations of perovskites' elasticities need to include possible
539 temperature variations within different regions of the mantle, especially those that are most likely to
540 be relevant to perovskite miscibility. Thirdly, the geophysical elasticity of a mechanical mixtures of
541 ca-pv and bdg will depend upon the geometry of each component in the mixture, and without
542 precise knowledge of these details any estimates will have large uncertainties. In spite of these
543 difficulties the difference in elasticity between miscible one-perovskite and a mechanically mixed
544 two-phase assemblage are estimated using static calculations (at 0 K) by adopting two major
545 approximations. The first approximation is that all errors associated with the calculation of ca-pv's
546 velocities (which remain unknown) cancel when considering only the velocity difference between
547 Ca-pv+bdg and a miscible perovskite. This assumption is justified by the observation that both sides

548 of the reaction contain CaO_{12} dodecahedrons, such that any errors resulting from calculations of
549 their elasticity are nullified. The second approximation is that the changes in elasticity induced by
550 phase miscibility occur primarily via changes to the static bulk (*K*) and shear (*G*) moduli, and that high
551 temperature phonons do not cause large relative changes to *K* or *G*. As shown in Table 1, static
552 calculations predict a density change resulting from miscibility that is close to an average of high
553 temperature results, such that it is not unreasonable to assume this assumption is justified. To
554 assess the third difficulty, that the geometry of mechanical mixtures of bdg and ca-pv remain
555 unknown, it is assumed that the Hashin-Shtrikman bounds provides the maximum and minimum
556 possible values of elasticity variations (Hashin and Shtrikman, 1963). The one-phase miscible
557 perovskite assemblage has no bounds, but its elasticity is compared with the upper and lower
558 bounds of the two phase mixture of bdg + ca-pv (Figure 5) so that the true elasticity difference must
559 lie between these bounds.

560 Employing these approximations a pyrolytic miscible one-phase perovskite (Ca# = 12.5)
561 possesses lower shear and compressional wave velocities ($-1.5 > \Delta V_s > -3.5\%$, , $-0.5 > \Delta V_p > -1.2\%$)
562 but a higher bulk sound speed ($0 < \Delta V_\Phi < 0.75\%$) compared to a two-phase mechanical mixture
563 (Figure 5). These velocity differences are potentially seismically relevant, possessing a similar
564 magnitude to those observations made within the LLSVPs, where a drop in V_s of 1-5% is associated
565 with little density variation and a possible anticorrelation of V_s-V_Φ (McNamara, 2019, Koelemeijer et
566 al., 2017). The magnitude of the predicted velocity variations increase with increasing Ca# at 125
567 GPa (Figure 6), such that ΔV_s and ΔV_p become more negative whilst ΔV_Φ increases. As Ca# appears
568 to exert a strong control on predicted velocity differences, compositions more enriched in calcium
569 including subducted basalt would possess a larger seismic signature associated with perovskite
570 miscibility if it occurs.

571 Whilst these static calculations provide some indication of the possible geophysical signature of
572 miscibility, stronger conclusions require further calculations to be performed at high temperature
573 and additional support for the assumptions we have made. Due to the difficulties in simulating and

574 measuring the elasticity of ca-pv, this may require dedicated high precision calculations or
575 appropriate experimental studies.
576
577 **5. Conclusion**
578 In this work we observe that ca-pv and bdg are unlikely to become miscible at conditions of the
579 lower mantle geotherm. At pressures of 25, 75 and 125 GPa we find the solubility of Ca in bdg to be
580 0.41/0.52/0.92 % at 2000 K and 0.72/1.07/3.30 % at 2500 K within the pure $MgSiO_3$-$CaSiO_3$ binary
581 system. Complete perovskite miscibility is potentially possible within pyrolytic bulk compositions
582 near the base of the mantle (> 90 GPa) in regions where temperatures are elevated, such as in an
583 LLSVPs. Descending slabs should possess two perovskite phases across all reasonable mantle
584 conditions.
585 Employing a simple model we demonstrate that only defects with large concentrations are likely
586 to affect the miscibility of lower mantle perovskites. We find that ferrous iron increases miscibility
587 but this is unlikely to be present in bridgmanite at conditions that lead to phase mixing due to
588 ferropericlase partitioning and mixtures of Fe and Al either make little change to miscibility or raise it
589 slightly. We predict phase mixing to have only a small effect on the formation of post-perovskite but
590 more work is needed. Harzburgitic compositions mix in the deep lower mantle with and basaltic
591 compositions remain unmixed throughout the lower mantle.
592 Perovskite miscibility may lead to small density decreases alongside seismically significant
593 changes of the shear wave speed when predictions for a single-phase perovskite solid solution are
594 compared with 2-perovskite mechanical mixtures. Additionally, our static calculations suggest an
595 anticorrelation of shear wave velocity and bulk sound speed may occur in regions where miscibility is
596 favourable. These predicted elasticity changes are similar to those observed within the LLSVPs,
597 which are also believed to be regions that possess super-adiabatic temperatures. Since regions of
598 elevated temperature are predicted to be those most likely to favour perovskite miscibility it is

feasible that this provides some explanation for the anomalous geophysical properties of these regions of the deep mantle.

Acknowledgments:

The research in this proposal was supported by National Natural Science Foundation of China (41773057). JM is highly thankful to Chinese Academy of Sciences (CAS) for PIFI. Calculations were run on the TH-2 High Performance Computer System in Lvliang, China.

Bibliography

ARMSTRONG, L. S., WALTER, M. J., TUFF, J. R., LORD, O. T., LENNIE, A. R., KLEPPE, A. K. & CLARK, S. M. 2012. Perovskite Phase Relations in the System CaO-MgO-TiO2-SiO2 and Implications for Deep Mantle Lithologies. *Journal of Petrology,* 53**,** 611-635.

CATALLI, K., SHIM, S.-H., DERA, P., PRAKAPENKA, V. B., ZHAO, J., STURHAHN, W., CHOW, P., XIAO, Y., CYNN, H. & EVANS, W. J. 2011. Effects of the Fe3+ spin transition on the properties of aluminous perovskite-New insights for lower-mantle seismic heterogeneities. *Earth and Planetary Science Letters,* 310**,** 293-302.

CREASY, N., GIRARD, J., ECKERT JR, J. O. & LEE, K. K. M. 2020. The Role of Redox on Bridgmanite Crystal Chemistry and Calcium Speciation in the Lower Mantle. 125**,** e2020JB020783.

EBERLE, M., GRASSET, O. & SOTIN, C. 2002. A numerical study of the interaction between the mantle wedge, subducting slab, and overriding plate. *Physics of the Earth and Planetary Interiors,* 134**,** 191-202.

FLYVBJERG, H. & PETERSEN, H. G. 1989. Error-estimates on averages of correlated data. *Journal of Chemical Physics,* 91**,** 461-466.

FUJINO, K., NISHIO-HAMANE, D., SUZUKI, K., IZUMI, H., SETO, Y. & NAGAI, T. 2009. Stability of the perovskite structure and possibility of the transition to the post-perovskite structure in CaSiO3, FeSiO3, MnSiO3 and CoSiO3. *Physics of the Earth and Planetary Interiors,* 177**,** 147-151.

FUJINO, K., SASAKI, Y., KOMORI, T., OGAWA, H., MIYAJIMA, N., SATA, N. & YAGI, T. 2004. Approach to the mineralogy of the lower mantle by a combined method of a laser-heated diamond anvil cell experiment and analytical electron microscopy. *Physics of the Earth and Planetary Interiors,* 143**,** 215-221.

GROCHOLSKI, B., CATALLI, K., SHIM, S.-H. & PRAKAPENKA, V. 2012. Mineralogical effects on the detectability of the postperovskite boundary. *Proceedings of the National Academy of Sciences of the United States of America,* 109**,** 2275-2279.

GU, T. T., LI, M. M., MCCAMMON, C. & LEE, K. K. M. 2016. Redox-induced lower mantle density contrast and effect on mantle structure and primitive oxygen. *Nature Geoscience,* 9**,** 723-+.

HASHIN, Z. & SHTRIKMAN, S. 1963. A VARIATIONAL APPROACH TO THE THEORY OF THE ELASTIC BEHAVIOUR OF MULTIPHASE MATERIALS. *Journal of the Mechanics and Physics of Solids,* 11**,** 127-140.

HIROSE, K. & FEI, Y. W. 2002. Subsolidus and melting phase relations of basaltic composition in the uppermost lower mantle. *Geochimica Et Cosmochimica Acta,* 66**,** 2099-2108.
HIROSE, K., SINMYO, R. & HERNLUND, J. 2017. Perovskite in Earth's deep interior. *Science,* 358**,** 734-738.
HIROSE, K., TAKAFUJI, N., SATA, N. & OHISHI, Y. 2005. Phase transition and density of subducted MORB crust in the lower mantle. *Earth and Planetary Science Letters,* 237**,** 239-251.
IRIFUNE, T., MIYASHITA, M., INOUE, T., ANDO, J., FUNAKOSHI, K. & UTSUMI, W. 2000. High-pressure phase transformation in CaMgSi2O6 and implications for origin of ultra-deep diamond inclusions. *Geophysical Research Letters,* 27**,** 3541-3544.
IRIFUNE, T. & RINGWOOD, A. E. 1993. PHASE-TRANSFORMATIONS IN SUBDUCTED OCEANIC-CRUST AND BUOYANCY RELATIONSHIPS AT DEPTHS OF 600-800 KM IN THE MANTLE. *Earth and Planetary Science Letters,* 117**,** 101-110.
IRIFUNE, T., SUSAKI, J., YAGI, T. & SAWAMOTO, H. 1989. PHASE-TRANSFORMATIONS IN DIOPSIDE CAMGSI2O6 AT PRESSURES UP TO 25-GPA. *Geophysical Research Letters,* 16**,** 187-190.
IRIFUNE, T. & TSUCHIDA, Y. 2007. Mineralogy of the Earth—Phase transitions and mineralogy of the lower mantle. *In:* GD, P. & G, S. (eds.) *Treatise on Geophysics, Vol 2 Mineral Physics.*
JUNG, D. Y. & SCHMIDT, M. W. 2011. Solid solution behaviour of CaSiO3 and MgSiO3 perovskites. *Physics and Chemistry of Minerals,* 38**,** 311-319.
KAMINSKI, F. 2017. *The Earth's Lower Mantle: Composition and Structure*, Springer International Publishing.
KAWAI, K. & TSUCHIYA, T. 2015. Small shear modulus of cubic CaSiO3 perovskite. *Geophysical Research Letters,* 42**,** 2718-2726.
KESSON, S. E., FITZ GERALD, J. D. & SHELLEY, J. M. 1998. Mineralogy and dynamics of a pyrolite lower mantle. *Nature,* 393**,** 252-255.
KOELEMEIJER, P., DEUSS, A. & RITSEMA, J. 2017. Density structure of Earth's lowermost mantle from Stoneley mode splitting observations. *Nature Communications,* 8.
KOMABAYASHI, T., HIROSE, K., SATA, N., OHISHI, Y. & DUBROVINSKY, L. S. 2007. Phase transition in CaSiO3 perovskite. *Earth and Planetary Science Letters,* 260**,** 564-569.
KRESSE, G. & FURTHMULLER, J. 1996a. Efficiency of ab-initio total energy calculations for metals and semiconductors using a plane-wave basis set. *Computational Materials Science,* 6**,** 15-50.
KRESSE, G. & FURTHMULLER, J. 1996b. Efficient iterative schemes for ab initio total-energy calculations using a plane-wave basis set. *Physical Review B,* 54**,** 11169-11186.
KRESSE, G. & JOUBERT, D. 1999. From ultrasoft pseudopotentials to the projector augmented-wave method. *Physical Review B,* 59**,** 1758-1775.
KUPENKO, I., MCCAMMON, C., SINMYO, R., PRESCHER, C., CHUMAKOV, A. I., KANTOR, A., RUEFFER, R. & DUBROVINSKY, L. 2014. Electronic spin state of Fe,Al-containing $MgSiO_3$ perovskite at lower mantle conditions. *Lithos,* 189**,** 167-172.
KURASHINA, T., HIROSE, K., ONO, S., SATA, N. & OHISHI, Y. 2004. Phase transition in Al-bearing CaSiO3 perovskite: implications for seismic discontinuities in the lower mantle. *Physics of the Earth and Planetary Interiors,* 145**,** 67-74.
MARQUARDT, H. & THOMSON, A. R. 2020. Experimental elasticity of Earth's deep mantle. *Nature Reviews Earth & Environment,* 1**,** 455-469.
MATTERN, E., MATAS, J., RICARD, Y. & BASS, J. 2005. Lower mantle composition and temperature from mineral physics and thermodynamic modelling. *Geophysical Journal International,* 160**,** 973-990.
MCNAMARA, A. K. 2019. A review of large low shear velocity provinces and ultra low velocity zones. *Tectonophysics,* 760**,** 199-220.
MICHAEL, P. J. & BONATTI, E. 1985. PERIDOTITE COMPOSITION FROM THE NORTH-ATLANTIC - REGIONAL AND TECTONIC VARIATIONS AND IMPLICATIONS FOR PARTIAL MELTING. *Earth and Planetary Science Letters,* 73**,** 91-104.

MOHN, C. & TRONNES, R. G. 2016. Iron spin state and site distribution in $FeAlO_3$-bearing bridgmanite. *Earth and Planetary Science Letters,* 440**,** 178-186.
MUIR, J. M. R. & BRODHOLT, J. P. 2016. Ferrous iron partitioning in the lower mantle. *Physics of the Earth and Planetary Interiors,* 257**,** 12-17.
O' NEILL, B. & JEANLOZ, R. 1990. EXPERIMENTAL PETROLOGY OF THE LOWER MANTLE - A NATURAL PERIDOTITE TAKEN TO 54 GPA. *Geophysical Research Letters,* 17**,** 1477-1480.
OGANOV, A. R. & ONO, S. 2004. Theoretical and experimental evidence for a post-perovskite phase of MgSiO3 in Earth's D '' layer. *Nature,* 430**,** 445-448.
OHTA, K., HIROSE, K., LAY, T., SATA, N. & OHISHI, Y. 2008. Phase transitions in pyrolite and MORB at lowermost mantle conditions: Implications for a MORB-rich pile above the core-mantle boundary. *Earth and Planetary Science Letters,* 267**,** 107-117.
ONO, S. 2008. Experimental constraints on the temperature profile in the lower mantle. *Physics of the Earth and Planetary Interiors,* 170**,** 267-273.
ONO, S., KIKEGAWA, T. & IIZUKA, T. 2004a. The equation of state of orthorhombic perovskite in a peridotitic mantle composition to 80 GPa: implications for chemical composition of the lower mantle. *Physics of the Earth and Planetary Interiors,* 145**,** 9-17.
ONO, S., OHISHI, Y. & MIBE, K. 2004b. Phase transition of Ca-perovskite and stability of Al-bearing Mg-perovskite in the lower mantle. *American Mineralogist,* 89**,** 1480-1485.
PRADHAN, G. K., FIQUET, G., SIEBERT, J., AUZENDE, A. L., MORARD, G., ANTONANGELI, D. & GARBARINO, G. 2015. Melting of MORB at core-mantle boundary. *Earth and Planetary Science Letters,* 431**,** 247-255.
RICOLLEAU, A., PERRILLAT, J.-P., FIQUET, G., DANIEL, I., MATAS, J., ADDAD, A., MENGUY, N., CARDON, H., MEZOUAR, M. & GUIGNOT, N. 2010. Phase relations and equation of state of a natural MORB: Implications for the density profile of subducted oceanic crust in the Earth's lower mantle. *Journal of Geophysical Research-Solid Earth,* 115.
RINGWOOD, A. E. 1991. PHASE-TRANSFORMATIONS AND THEIR BEARING ON THE CONSTITUTION AND DYNAMICS OF THE MANTLE. *Geochimica Et Cosmochimica Acta,* 55**,** 2083-2110.
SHIM, S. H., GROCHOLSKI, B., YE, Y., ALP, E. E., XU, S. Z., MORGAN, D., MENG, Y. & PRAKAPENKA, V. B. 2017. Stability of ferrous-iron-rich bridgmanite under reducing midmantle conditions. *Proceedings of the National Academy of Sciences of the United States of America,* 114**,** 6468-6473.
SHIM, S. H., JEANLOZ, R. & DUFFY, T. S. 2002. Tetragonal structure of CaSiO3 perovskite above 20 GPa. *Geophysical Research Letters,* 29.
STIXRUDE, L., LITHGOW-BERTELLONI, C., KIEFER, B. & FUMAGALLI, P. 2007. Phase stability and shear softening in CaSiO3 perovskite at high pressure. *Physical Review B,* 75.
SUN, T., ZHANG, D. B. & WENTZCOVITCH, R. M. 2014. Dynamic stabilization of cubic CaSiO3 perovskite at high temperatures and pressures from ab initio molecular dynamics. *Physical Review B,* 89**,** 094109-1.
TAMAI, H. & YAGI, T. 1989. HIGH-PRESSURE AND HIGH-TEMPERATURE PHASE-RELATIONS IN CASIO3 AND CAMGSI2O6 AND ELASTICITY OF PEROVSKITE-TYPE CASIO3. *Physics of the Earth and Planetary Interiors,* 54**,** 370-377.
TATENO, S., HIROSE, K., SATA, N. & OHISHI, Y. 2009. Determination of post-perovskite phase transition boundary up to 4400 K and implications for thermal structure in D '' layer. *Earth and Planetary Science Letters,* 277**,** 130-136.
THOMSON, A. R., CRICHTON, W. A., BRODHOLT, J. P., WOOD, I. G., SIERSCH, N. C., MUIR, J. M. R., DOBSON, D. P. & HUNT, S. A. 2019. Seismic velocities of CaSiO3 perovskite can explain LLSVPs in Earth's lower mantle. *Nature,* 572**,** 643-+.
UCHIDA, T., WANG, Y., NISHIYAMA, N., FUNAKOSHI, K., KANEKO, H., NOZAWA, A., VON DREELE, R. B., RIVERS, M. L., SUTTON, S. R., YAMADA, A., KUNIMOTO, T., IRIFUNE, T., INOUE, T. & LI, B. S. 2009. Non-cubic crystal symmetry of CaSiO3 perovskite up to 18 GPa and 1600 K. *Earth and Planetary Science Letters,* 282**,** 268-274.

VITOS, L., MAGYARI-KOPE, B., AHUJA, R., KOLLAR, J., GRIMVALL, G. & JOHANSSON, B. 2006. Phase transformations between garnet and perovskite phases in the Earth's mantle: A theoretical study. *Physics of the Earth and Planetary Interiors,* 156**,** 108-116.

XU, S. Z., LIN, J. F. & MORGAN, D. 2017. Iron partitioning between ferropericlase and bridgmanite in the Earth's lower mantle. *Journal of Geophysical Research-Solid Earth,* 122**,** 1074-1087.

YE, Y., SHIM, S. H., PRAKAPENKA, V. & MENG, Y. 2018. Equation of state of solid Ne inter-calibrated with the MgO, Au, Pt, NaCl-B2, and ruby pressure scales up to 130GPa. *High Pressure Research,* 38**,** 377-395.

ZHANG, Z., STIXRUDE, L. & BRODHOLT, J. 2013. Elastic properties of MgSiO3-perovskite under lower mantle conditions and the composition of the deep Earth. *Earth and Planetary Science Letters,* 379**,** 1-12.

753

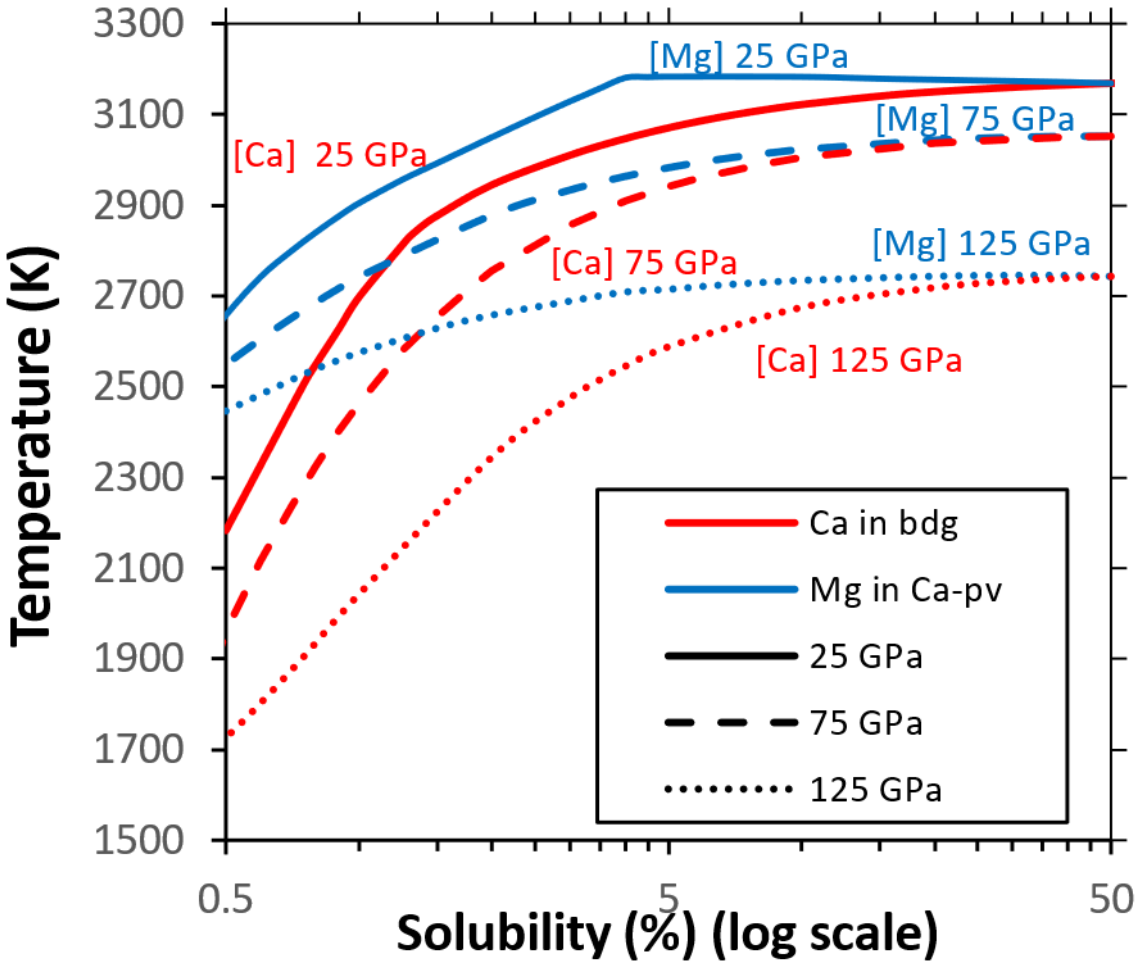

754

755

756 Figure 1: Solubility of Mg in Ca-pv (blue) and Ca in bdg (red) as a function of temperature and
757 pressure (solid lines=25 Gpa, dashed=75, dotted=125). The plateau after the graph levels off is the
758 temperature where all ratios of Ca-pv and bdg are miscible into a single phase. This graph is
759 presented with log solubility to demonstrate the low solubility behaviour clearly, a more traditional
760 phase diagram is presented in Figure S3.

761

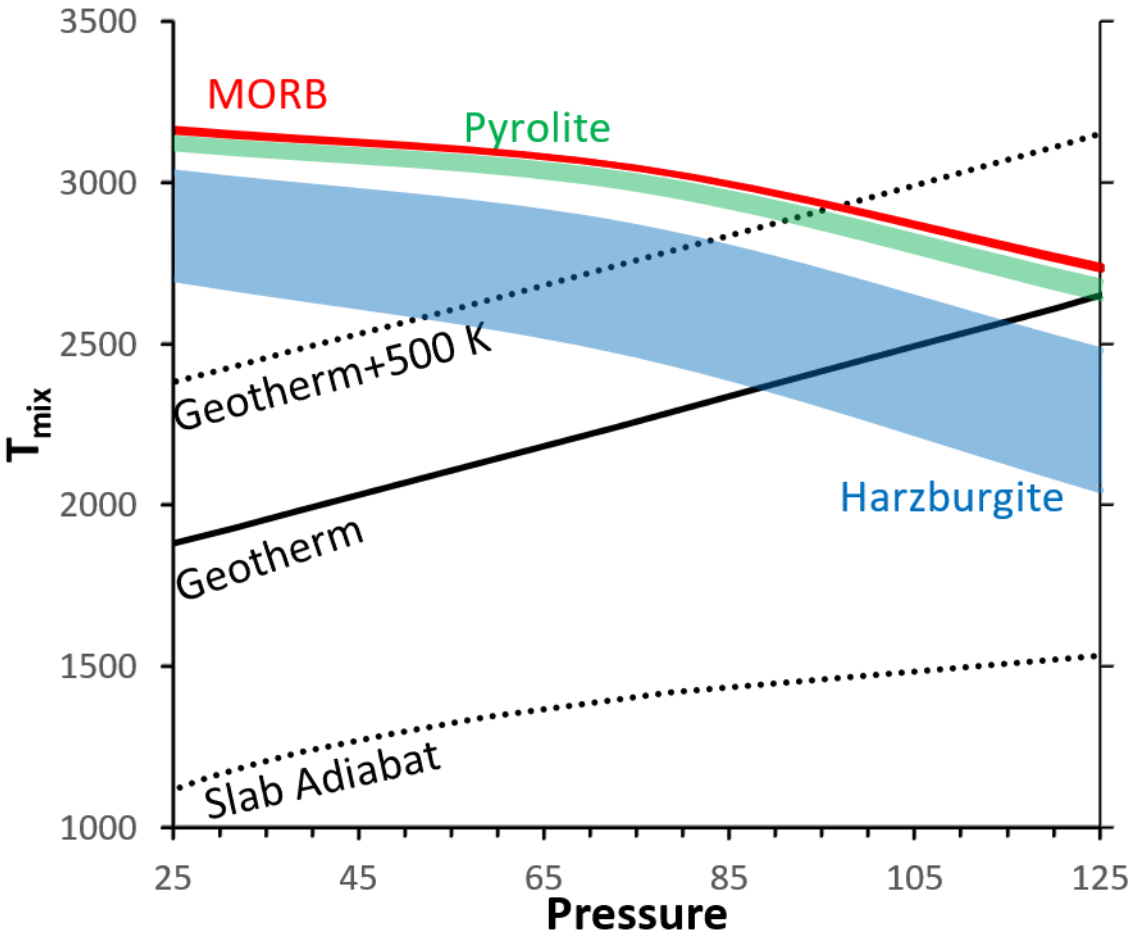

Figure 2: Projected T_{mix} for a pyrolytic (Ca#=8-12), MORB (Ca#=30-60) and harzburgitic (Ca#=1-3) composition with no defect elements. In each case the bounds represent the Ca# range with the lower bound of T_{mix} corresponding to the lowest amount of Ca and the higher bound to the highest. Shown on the graph are a lower mantle geotherm (Ono, 2008), the coldest possible slab adiabat (Eberle et al., 2002) and an artificial "hot" geotherm representing hot spots in the lower mantle that is the geotherm+500 K.

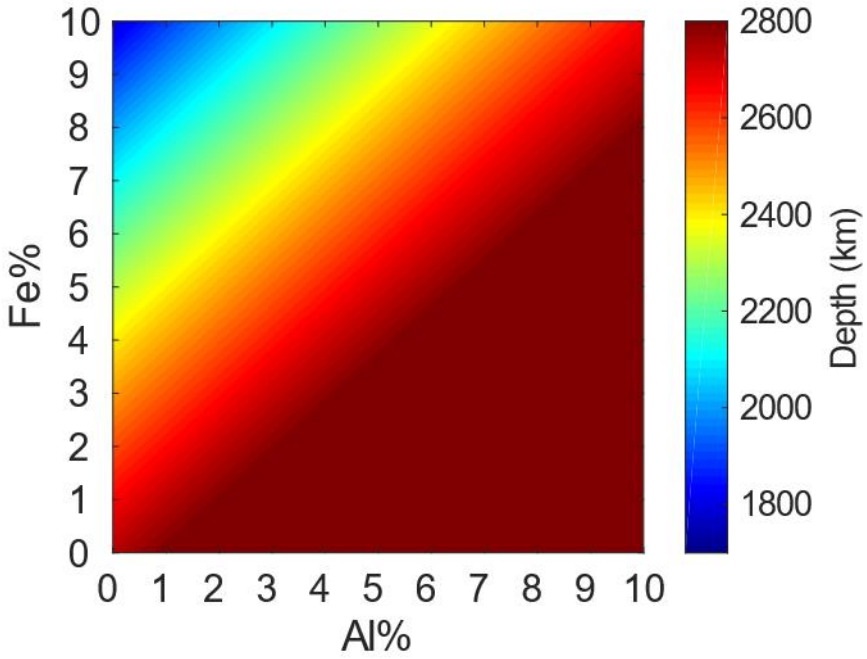

Figure 3: Depth at which T_{mix} crosses the geotherm for a pyrolytic (Ca#=10) mixture with various amounts of Fe and Al as determined via the model outlined in the text. For this model the formation of Fe-Al was prioritised such that Fe-Al forms first and then leftover Fe or Al forms Ferrous iron or Al-Al pairs. Mixing depths above 1800 km and below 2800 km have been truncated to these values to follow the stability field of bdg.

779

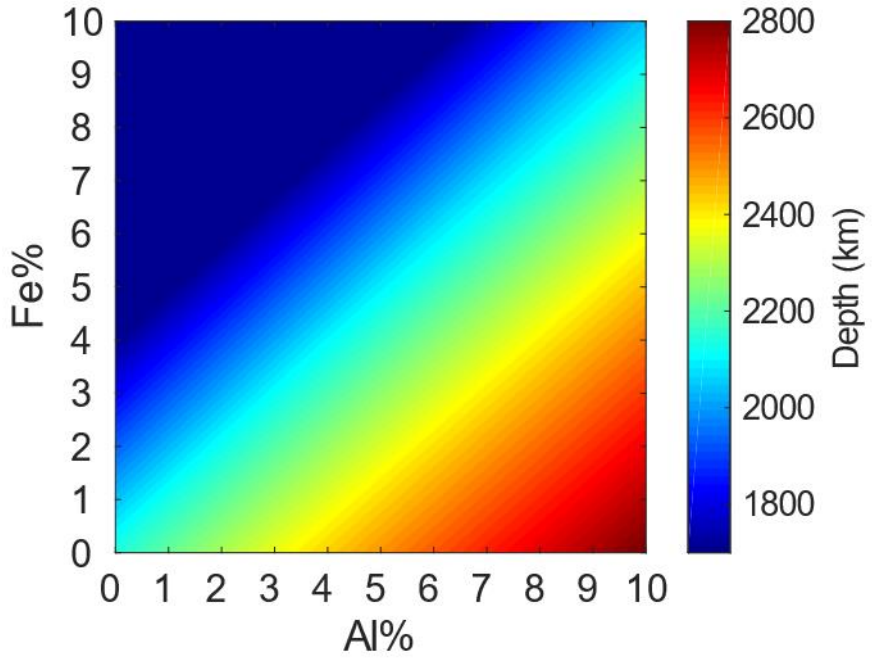

780

781 Figure 4: As Figure 3 but for a “hot” geotherm (geotherm+500 K).

782

783

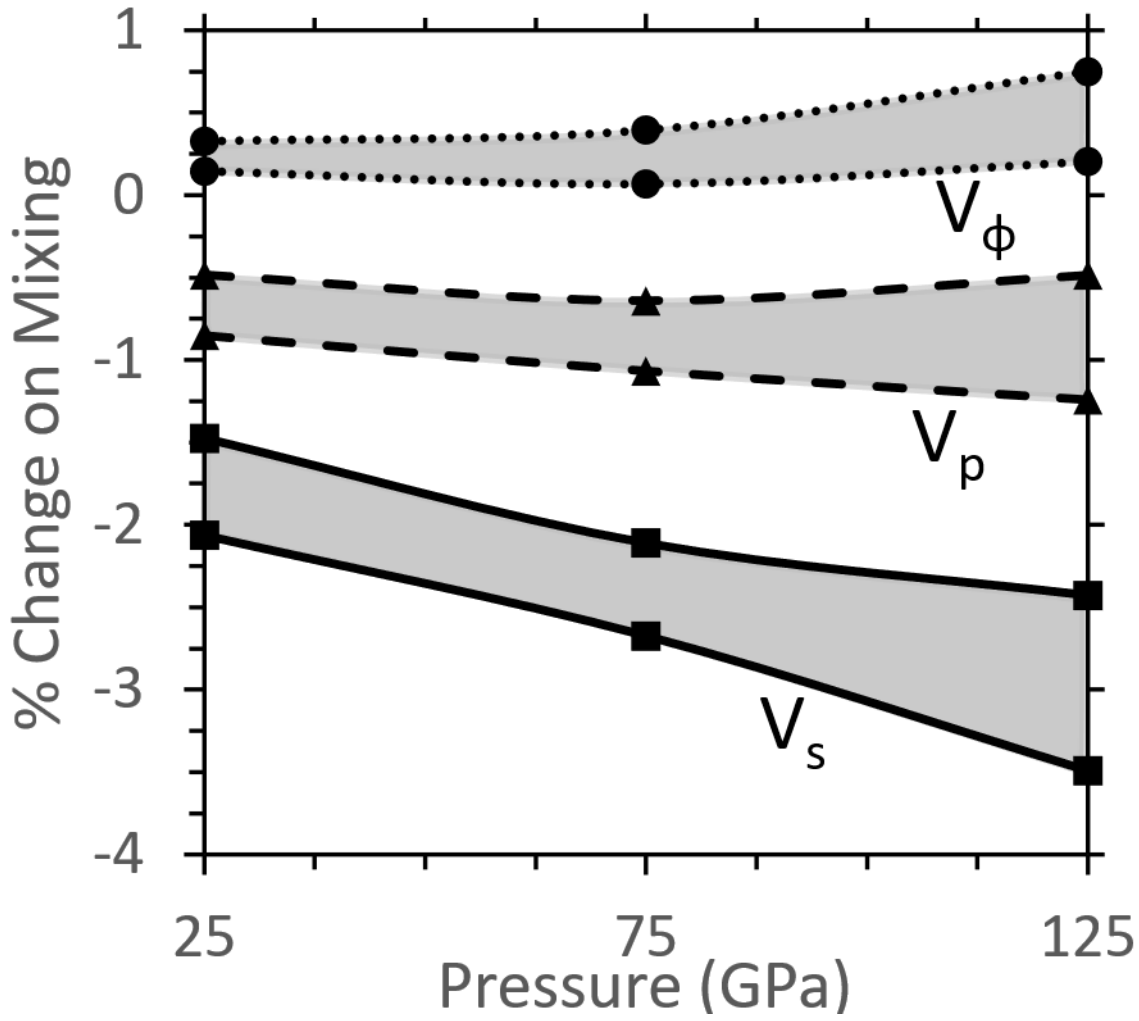

784

785 Figure 5: Plot of the change in V_s (solid lines), V_p (dashed lines), V_Φ (dotted black lines) on
786 converting from a mechanical mixture of Ca-pv and bdg to a single phase calculated directly at
787 Ca#=12.5. These calculations were run at static conditions (~0 K) and 25, 75 and 125 GPa. Ca-pv
788 elasticity was determined in the i4mcm phase, bdg and the mixed phase in the pbnm phase. To
789 determine the elasticity of a mechanical mixture of Ca-pv and bdg we used the Hashin-Shtikman
790 bounds (Hashin and Shtrikman, 1963) which are the bounds pictured, the elasticity change upon
791 mixing must fall between these bounds.

792

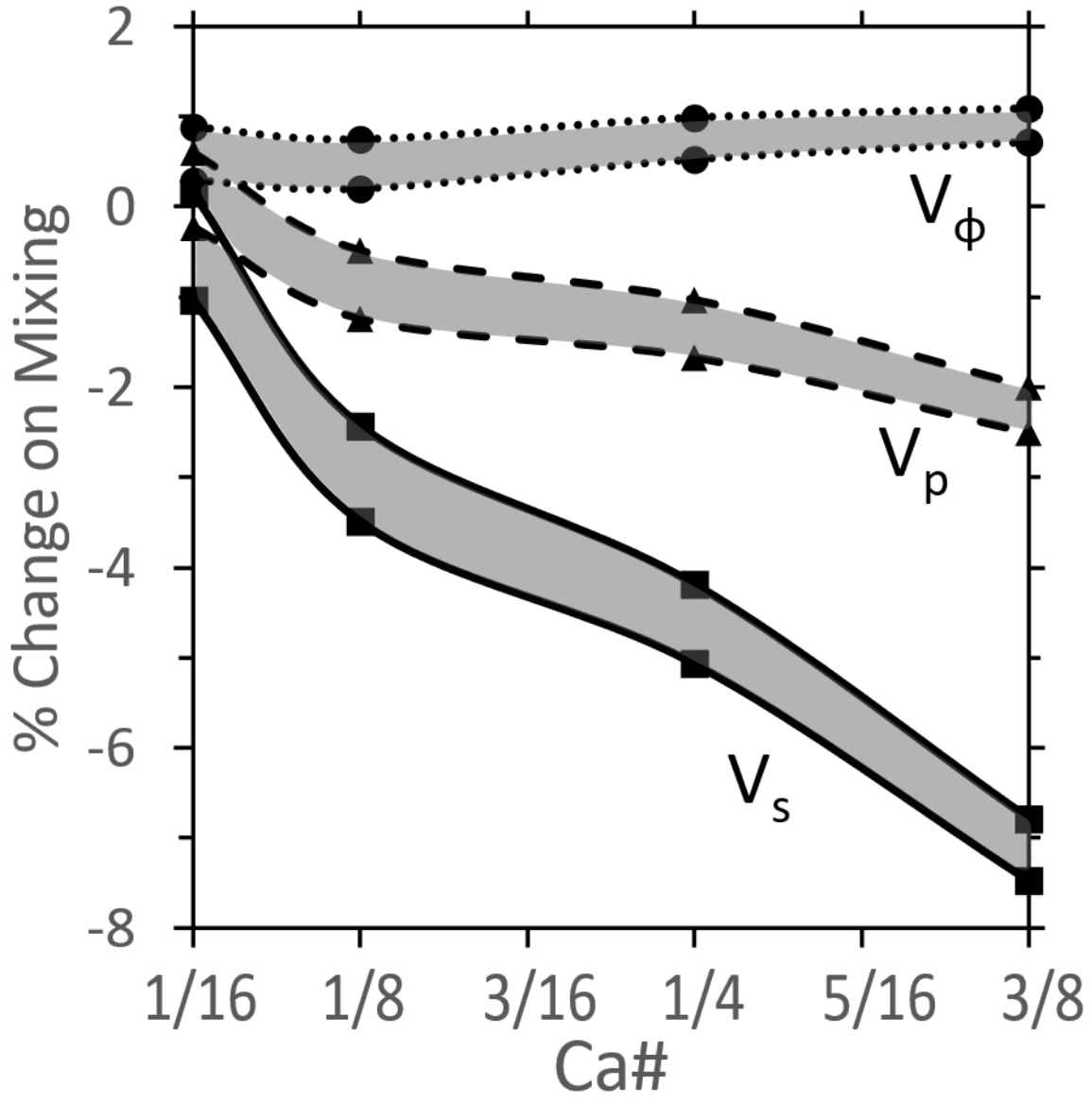

Figure 6: As Figure 5 but showing the variation in elasticity with varied Ca# at 125 GPa. The x axis shows the amount of Ca (x) in Mg16-xCaxSi16O48 such that x=1 refers to Ca

800

801 Tables

802 Table 1: Change in density on forming a mixed phase for Ca#=50 (determined from MD) and 12.5
803 (extrapolated from MD values at Ca#=25 and 50) at various pressures and temperatures.

804 Table 2: Effect of various elements on T_{mix} at 25 and 125 GPa with Ca#=10% (Ca#=50 and 90
805 values are in Table S2 and S3) which is a roughly pyrolytic mixture. Columns are name of the
806 element, site at which that element was placed (A=Mg site, B= Si site, AB= 1 element at each,
807 Int=interstitial), the change in ΔH_{mix} in eV from placing one defect element, proportion of this
808 element (K) in the Ca-pv before mixing (1 is all in Ca-pv, 0 is all in bdg) and then the next 3 columns
809 are the change in T_{mix} in K with 0.1, 1 and 10 atomic % (of bridgmanite) of the element in questions.
810 All elements are non-spin polarised except those labelled HS which were run with their standard
811 high spin configuration. 2H represents a water molecule where a Mg has been replaced with 2
812 Hydrogens in the vacancy. Fe-Al represents a high spin ferric iron replacing a Mg and an Al replacing
813 a Si.

814 Table 3: Change in vibrational entropy (defined as ΔS_{vib} (iron containing supercell) - ΔS_{vib} (iron
815 free supercell) from replacing 1 Mg with 1 Fe atom in $Mg_{16}Si_{16}O_{48}$ or Mg_8Ca_8 $Si_{16}O_{48}$ (Fe%=6.25) and
816 the difference to the energy of reaction 1. The equivalent change induced to enthalpy by iron under
817 the same conditions is -1.94 and -6.04 meV/atom at 25 and 125 GPa respectively. Thus at small
818 pressures this vibrational entropy term borders on significance but at high pressures where mixing
819 occurs it is negligible and well below other sources of error in DFT.

820

821

822

	Ca#=0.125			Ca#=0.5		
	25 GPa	75 GPa	125 GPa	25 GPa	75 GPa	125 GPa
Static	-0.48	-0.41	-0.28	-0.74	-0.75	-0.79
1000 K	-0.15	-0.17	-0.18	-0.59	-0.69	-0.73
2000	-0.19	-0.19	-0.19	-0.76	-0.77	-0.75
3000	-0.25	-0.23	-0.19	-0.98	-0.93	-0.76

823

824 Table 1: Change in density on forming a mixed phase for Ca#=0.5 (determined from MD) and 0.125
825 (extrapolated from MD values at Ca#=0.25 and 0.5) at various pressures and temperatures.

826

827

828

		25 GPa					125 GPa				
Element	Site	ΔH_{mix}	K	0.10%	1	10	ΔH_{mix}	K	0.10%	1	10
2H	A	0.11	0	2	16	148	0.95	0	13	134	1224
He	Int	-0.27	1	-23	-233	-1883	0.07	1	-7	-70	-628
Ne	Int	-0.86	1	-39	-389	-3453	-0.90	1	-21	-213	-1839
Li(I)	A	0.28	0	6	60	538	0.76	0	11	106	981
Na(I)	A	-0.42	0	-12	-125	-1412	-0.53	0	-9	-86	-883
K(I)	A	-0.10	1	-32	-305	-2057	-0.16	1	-17	-162	-1301
Be(II)	A	0.18	0	3	34	311	1.17	0	17	166	1505
Cu(II)	A	-0.14	0	-5	-51	-526	-0.38	0	-6	-64	-646
Ni(II)	A	-0.39	0	-11	-116	-1292	-0.47	0	-8	-77	-791
Zn(II)	A	-0.13	0	-5	-47	-477	-0.43	0	-7	-71	-722
Co(II)	A	-0.42	0	-12	-124	-1400	-0.55	0	-9	-89	-921
Fe(II)	A	-0.31	0	-9	-95	-1029	-0.48	0	-8	-79	-811
Fe(II)HS	A	**-0.20**	**0**	**-7**	**-65**	**-682**	**-0.47**	**0**	**-8**	**-76**	**-783**
V(II)	A	-0.26	0	-8	-82	-875	-0.45	0	-7	-74	-761
Cr(II)	A	0.09	0	1	9	82	-0.23	0	-4	-41	-417
Mn(II)	A	0.25	0	5	52	473	0.14	0	1	15	140
Sc(II)	A	-0.22	1	-35	-336	-2244	-0.07	1	-15	-150	-1216
Sc(II) HS	A	-0.26	1	-36	-347	-2313	-0.60	1	-1	-7	-67
Sr(II)	A	0.51	1	-16	-153	-1193	0.70	1	-4	-39	-491
Ba(II)	A	0.98	1	-4	-38	-581	1.38	1	6	57	114
B(III)	AB	0.62	1	15	147	1253	-0.77	1	-12	-123	-1294
Al(III)	AB	0.24	**0**	**5**	**48**	**439**	**0.43**	**0**	**6**	**58**	**550**
Cr(III)	AB	-0.17	1	0	-4	-44	0.07	1	0	5	44
Cr(III)Hs	AB	0.14	1	2	23	218	-0.15	1	-3	-29	-289
Ga(III)	AB	0.13	0	2	20	185	0.34	0	4	44	419
Fe(III)	AB	0.79	0	19	188	1569	1.03	0	15	146	1337
Fe(III)HS	AB	0.01	**0**	**-1**	**-10**	**-96**	**0.18**	**0**	**2**	**20**	**189**
Sc(III)	AB	-0.20	0	-6	-65	-673	-0.07	**0**	-2	-17	-167
In(III)	AB	-0.07	0	-3	-32	-322	0.17	0	2	19	182
Fe-Al	AB	0.02	**0**	**-1**	**-7**	**-74**	**0.00**	**0**	**-1**	**-7**	**-71**
C 4+	B	-0.51	1	-15	-148	-1753	-0.08	0	-2	-19	-193
S 4+	B	-0.45	0	-13	-133	-1530	-0.21	0	-4	-38	-387
Ge4+	B	-0.17	0	-6	-57	-587	-0.09	0	-2	-20	-204
Sn4+	B	-0.51	0	-15	-150	-1780	-0.38	0	-6	-63	-645
Ti4+	B	-0.07	1	-3	-32	-329	-0.26	0	-4	-45	-452

829 Table 2: Effect of various elements on T_{mix} at 25 and 125 GPa with Ca#=0.1 (Ca#=0.5 and 0.9 values
830 are in Table S6 and S7) which is a roughly pyrolytic mixture. Columns are name of the element, site
831 at which that element was placed (A=Mg site, B= Si site, AB= 1 element at each, Int=interstitial), the
832 change in ΔH_{mix} in eV from placing one defect element, proportion of this element (K) in the Ca-pv

before mixing (1 is all in Ca-pv, 0 is all in bdg) and then the next 3 columns are the change in T_{mix} in K with 0.1, 1 and 10 atomic % (of bridgmanite) of the element in questions. All elements are non-spin polarised except those labelled HS which were run with their standard high spin configuration. 2H represents a water molecule where a Mg has been replaced with 2 Hydrogens in the vacancy. Fe-Al represents a high spin ferric iron replacing a Mg and an Al replacing a Si.

		ΔS_{vibFe} (meV/atom)		
Pressure	Temperature	bridgmanite	mixed phase	Difference
25 GPa	1000 K	-2.6	-0.3	2.3
	2000 K	-2.2	-0.1	2.1
	3000 K	-1.6	-0.3	1.3
125 GPa	1000 K	-4.1	-4	0.1
	2000 K	-4.0	-3.9	0.1
	3000 K	-3.8	-4.4	-0.6

Table 3: Change in vibrational entropy (defined as ΔS_{vib} (iron containined supercell) - ΔS_{vib} (iron free supercell) from replacing 1 Mg with 1 Fe atom in $Mg_{16}Si_{16}O_{48}$ or $Mg_8Ca_8\ Si_{16}O_{48}$ (Fe%=6.25) and the difference to the energy of reaction 1. The equivalent change induced to enthalpy by iron under the same conditions is -1.94 and -6.04 meV/atom at 25 and 125 GPa respectively. Thus at small pressures this vibrational entropy term borders on significance but at high pressures where mixing occurs it is neglible and well below other sources of error in DFT.